ChemComm

COMMUNICATION

Check for updates

Enhanced oxygen storage capacity of cation-ordered cerium–zirconium oxide induced by titanium substitution†

Yoshihiro Goto, iD *[a] Akira Morikawa, iD [a] Masaoki Iwasaki,[a] Masahide Miura[b] and Toshitaka Tanabe[a]

Herein, we report on the synthesis of $Ce_{0.5}Zr_{0.5-x}Ti_xO_2$ oxygen storage materials prepared *via* a solution combustion method. $Ce_{0.5}Zr_{0.4}Ti_{0.1}O_2$ showed an outstanding oxygen storage capacity (1310 μmol-O per g) at 200 °C compared to conventional κ-$Ce_2Zr_2O_8$ (650 μmol-O per g) due to its cation ordering and the formation of weakly bound oxygen atoms induced by Ti substitution.

Some metal oxides can reversibly store/release oxygen or control the oxygen concentration in the gas phase in response to changes in the temperature and oxygen partial pressure.[1] Such oxides have been actively investigated for different applications in the fields of energy conversion and environmental protection such as solid oxide fuel cells (SOFCs),[2] thermochemical water splitting,[3] and water–gas shift reactions.[4] Ceria (CeO_2) is generally used as an oxygen storage material in automotive exhaust catalysis in order to maintain the high purification efficiency by precisely controlling the oxygen partial pressure.[5,6]

The oxygen storage/release capacity (OSC) of CeO_2 corresponding to the redox reaction between Ce^{3+} and Ce^{4+} is greatly enhanced by Zr substitution, reaching its maximum for $Ce_{0.5}Zr_{0.5}O_2$ (900 μmol-O per g at 500 °C).[1a] High-temperature reduction (in H_2 or CO at 1200 °C) of $Ce_{0.5}Zr_{0.5}O_2$ yields the $Ce_2Zr_2O_7$ pyrochlore (Ce and Zr site ordered $Ce_{0.5}Zr_{0.5}O_{1.75}$), which leads to cation-ordered $Ce_{0.5}Zr_{0.5}O_2$ after a re-oxidation treatment.[7–9] This cation-ordered $Ce_{0.5}Zr_{0.5}O_2$ (referred to as κ-$Ce_2Zr_2O_8$) shows an outstanding OSC of 1500 μmol-O per g at 500 °C, where almost all Ce atoms in κ-$Ce_2Zr_2O_8$ (89%) contribute to the $Ce^{3+} \leftrightarrow Ce^{4+}$ redox conversion.[9,10] Such a high OSC value is derived from the topotactic transformation of the κ-$Ce_2Zr_2O_8$ into $Ce_2Zr_2O_7$ pyrochlore assessed by the first-principles calculation method.[11]

The cation ordering in complex oxides is often induced by cation size mismatches.[12–14] Therefore, an increase in the cation size mismatch from 1.15 (Ce^{4+}/Zr^{4+}) to 1.58 (Ce^{3+}/Zr^{4+}) should stabilize the cation-ordered structure of the $Ce_2Zr_2O_7$ pyrochlore. Thus, the substitution of Zr^{4+} (0.84 Å) with Ti^{4+} (0.74 Å) in $Ce_{0.5}Zr_{0.5}O_2$ would result in cation-ordered $Ce_{0.5}Zr_{0.5-x}Ti_xO_2$ due to the expansion of the mismatch against Ce^{4+} (0.97 Å).[15] However, conventional methods such as solid state reactions and co-precipitations are not able to achieve homogeneous Ti distribution.

In this study, we employed a solution combustion method that is characterized as a self-sustained exothermic reaction.[16–18] Technically, the combustion of fuels (*e.g.* urea, glycine, *etc.*) with oxidants (typically metal nitrates) followed by a rapid quenching allowed us to obtain homogeneous compounds with desired compositions.[19,20] Also, the Ti substitution in $Ce_{0.5}Zr_{0.5-x}Ti_xO_2$ ($0 \leq x \leq 0.2$) induced pyrochlore-type cation ordering between the Ce and Zr sites and greatly increased the OSC values. The OSC of $Ce_{0.5}Zr_{0.4}Ti_{0.1}O_2$ (1310 μmol-O per g) was found to be approximately twice that of κ-$Ce_2Zr_2O_8$ (650 μmol-O per g) at a lower temperature (200 °C). Moreover, the origins of the cation ordering and enhanced OSC were investigated from the viewpoints of crystal structures and the strengths of the bonds between the oxygen atoms and the surrounding cations.

The $Ce_{0.5}Zr_{0.5-x}Ti_xO_2$ samples were prepared from aqueous solutions containing both glycine as a fuel and the respective metal nitrates as oxidants. The solutions with cation ratios of Ce : Zr : Ti = 0.5 : (0.5 − x) : x (x = 0, 0.1, 0.2, 0.3, 0.4, and 0.5) were burned by heating up to 400 °C, resulting in light-yellow powders (experimental details are provided in the ESI†). The specific surface areas (SSAs) of the Ti-containing samples (x = 0.1 : 8.29 m² g⁻¹, x = 0.2 : 7.48 m² g⁻¹) were less than half of the amount of x = 0 (17.08 m² g⁻¹). However, these SSAs were much higher than that of κ-$Ce_2Zr_2O_8$ (0.35 m² g⁻¹), which was obtained by a high-temperature reduction of $Ce_{0.5}Zr_{0.5}O_2$ at 1200 °C followed by oxidation at 500 °C (Table 1).

A cubic phase was observed in the X-ray diffraction (XRD) patterns of x = 0, 0.1, and 0.2 (Fig. 1a). An unknown impurity with a reflection at around $2\theta = 26.7°$ was found, but its intensity

[a] *Toyota Central R&D Labs., Inc., 41-1 Nagakute, Aichi 480-1192, Japan.*
 E-mail: yoshihiro-goto@mosk.tytlabs.co.jp

[b] *Toyota Motor Corporation, Toyota, Aichi 471-8571, Japan*

† Electronic supplementary information (ESI) available: Experimental details, XRD patterns, XANES spectra, crystal structures, TGA curves, crystallographic information, and BVS parameters. See DOI: 10.1039/c8cc01308j

Table 1 Physical characteristics of $Ce_{0.5}Zr_{0.5-x}Ti_xO_2$ and κ-$Ce_2Zr_2O_8$

Compound	SSA^a (m^2 g^{-1})	Space group	Cell volume^b (Å)	Cation ratio^c (mol%)			OSC^d (μmol-O per g)		
				Ce	Zr	Ti	200 °C	400 °C	600 °C
$Ce_{0.5}Zr_{0.5}O_2$	17.08	$Fm\bar{3}m$	146.167(5)	50.2	49.8	—	910	1070	1120
$Ce_{0.5}Zr_{0.4}Ti_{0.1}O_2$	8.29	$F\bar{4}3m$	144.729(3)	50.3	40.0	9.7	1310	1530	1530
$Ce_{0.5}Zr_{0.3}Ti_{0.2}O_2$	7.48	$F\bar{4}3m$	143.598(4)	50.2	30.1	19.7	1370	1550	1590
κ-$Ce_2Zr_2O_8$^{e}	0.35	$P2_13$	145.758(5)	(50)^f	(50)^f	—	650	1530	1560

^{a} Measured by BET analysis. ^{b} Calculated from the lattice parameters based on the unit cell of $Ce_{0.5}Zr_{0.5}O_2$ ($Z = 4$). ^{c} Measured by ICP-OES. ^{d} Estimated from the weight losses in the TGA curves. ^{e} Prepared by the reduction of $Ce_{0.5}Zr_{0.5}O_2$ at 1200 °C followed by oxidation at 500 °C.[9] ^{f} Feed ratio in the synthesis.

was less than 1% of the main cubic phase. Additional phases (CeO_2 and unknown) were found in the patterns of $x = 0.3, 0.4$, and 0.5 (Fig. S1, ESI†). The main phase of $x = 0$ was characterized by a cubic fluorite structure ($Fm\bar{3}m$) with $a = 5.2682(2)$ Å, which was in agreement with the reported space group ($Fm\bar{3}m$) and lattice parameter ($a = 5.269$) of $Ce_{0.5}Zr_{0.5}O_2$.[21] In contrast, the main phases of $x = 0.1$ and 0.2 showed additional peaks originating from their superstructures assigned to a $2 \times 2 \times 2$ supercell based on $Ce_{0.5}Zr_{0.5}O_2$. The cell volumes calculated from the lattice parameters showed a linear decrease with an increase in the value of x (Fig. 1b and Table 1). The volume reduction indicated the formation of $Ce_{0.5}Zr_{0.5-x}Ti_xO_2$ solid solutions ($0 \leq x \leq 0.2$) because the ionic radius of tetravalent Ti (0.74 Å) is smaller than that of Zr (0.84 Å).[15] Elemental analysis using inductively coupled plasma-optical emission spectrometry (ICP-OES) supported the formation of the solid solution since the measured compositions of the obtained $Ce_{0.5}Zr_{0.5-x}Ti_xO_2$ samples were equal to the feed ratios of Ce:Zr:Ti = 5:5:0, 5:4:1, and 5:3:2 for $x = 0, 0.1$, and 0.2, respectively (Table 1).

Rietveld refinement of the synchrotron XRD pattern of $Ce_{0.5}Zr_{0.4}Ti_{0.1}O_2$ was performed using a $F\bar{4}3m$ model in which Ce and Zr(Ti) atoms were ordered along the $\langle 110 \rangle$ direction (Fig. 2a). The high reliability of the refined data ($R_{wp} = 6.46\%$, goodness of fit = 0.80, Table S1, ESI†) suggested that the predicted model for $Ce_{0.5}Zr_{0.4}Ti_{0.1}O_2$ was reasonable. The crystal structure is shown in Fig. 2a. The electron diffraction (ED) patterns of the [100], [110], and [111] zone axes for $Ce_{0.5}Zr_{0.4}Ti_{0.1}O_2$ ($x = 0.1$) were indexed to the space group $F\bar{4}3m$ (Fig. 2b), which was consistent

with the structural model used in the Rietveld refinement. Moreover, the absence of 110, 211, and 330 reflections excluded the space group $P2_13$, which could be derived from the slight displacements of some O sites from the ideal positions as observed in κ-$Ce_2Zr_2O_8$.[10] This indicates that the structure of $Ce_{0.5}Zr_{0.4}Ti_{0.1}O_2$ was less distorted than that of κ-$Ce_2Zr_2O_8$.

The results from the XRD and ED measurements suggested that pyrochlore-type cation ordering in the $Ce_{0.5}Zr_{0.5-x}Ti_xO_2$ fluorite was observed above a cation size mismatch ($r_{Ce^{4+}}/r_{Zr^{4+}(Ti^{4+})}$) of 1.18, where $r_{Zr^{4+}(Ti^{4+})}$ denotes the weighted average of ionic radii for Zr^{4+} and Ti^{4+}. In contrast, cation ordering in the $A_{0.5}B_{0.5}O_{1.75}$ defect fluorite (e.g. $Gd_{0.5}Zr_{0.5-x}Ce_xO_{1.75}$ and $Y_{0.5}Ti_{0.5-x}Zr_xO_{1.75}$) is generally observed above 1.23,[12,13] which is slightly larger than the value for the $Ce_{0.5}Zr_{0.5-x}Ti_xO_2$ fluorite (1.18). This difference suggests that the absence of oxygen defect enabled cation ordering in the $A_{0.5}B_{0.5}O_2$ fluorite with a smaller cation size mismatch.

Fig. 2 (a) Structural characterization of $Ce_{0.5}Zr_{0.4}Ti_{0.1}O_2$ obtained via Rietveld refinement of the synchrotron XRD data at room temperature. The red crosses, green solid line, and blue solid line represent the observed, calculated, and different intensities, respectively. The black ticks show the peak positions. The inset displays the crystal structure of $Ce_{0.5}Zr_{0.4}Ti_{0.1}O_2$ with the space group $F\bar{4}3m$. The orange, green, blue, and red spheres represent Ce, Zr, Ti, and O, respectively. (b) ED patterns for $Ce_{0.5}Zr_{0.4}Ti_{0.1}O_2$ projected along the [100], [110], and [111] axes, indexed constantly to the $F\bar{4}3m$ space group.

Fig. 1 (a) XRD patterns of $Ce_{0.5}Zr_{0.5-x}Ti_xO_2$. Black, red, and blue solid lines represent the patterns of $x = 0, 0.1$, and 0.2, respectively. Hashtags (#), asterisks (*), and black squares (◆) indicate peaks arising from the main cubic phase, their superstructure, and unknown impurity, respectively. (b) Cell volumes of $Ce_{0.5}Zr_{0.5-x}Ti_xO_2$ based on the unit cell of $Ce_{0.5}Zr_{0.5}O_2$ ($Z = 4$).
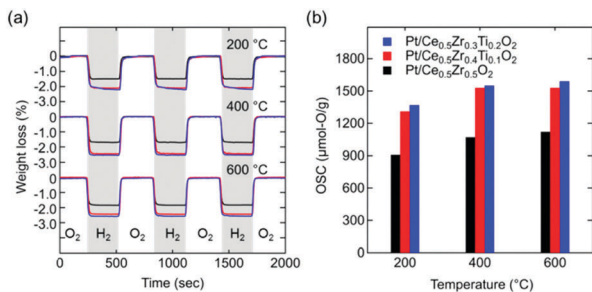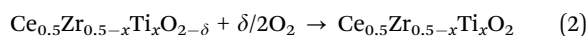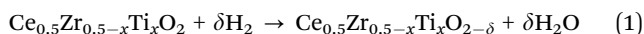
Fig. 3 (a) TGA curves of $Pt/Ce_{0.5}Zr_{0.5-x}Ti_xO_2$ upon switching between 5% O_2/N_2 and 5% H_2/N_2 every 5 min at various temperatures. (b) Estimated OSCs. Black, red, and blue lines and columns represent $Pt/Ce_{0.5}Zr_{0.5}O_2$, $Pt/Ce_{0.5}Zr_{0.4}Ti_{0.1}O_2$, and $Pt/Ce_{0.5}Zr_{0.3}Ti_{0.2}O_2$, respectively.

Fig. 4 (a) Ce L_3-edge XANES spectra of $Pt/Ce_{0.5}Zr_{0.5}O_2$ (black lines) and $Pt/Ce_{0.5}Zr_{0.4}Ti_{0.1}O_2$ (red lines) in 3% O_2/He (dashed lines) and 3% H_2/He (solid lines) at 600 °C. Peaks A_1 and A_2 were assigned to Ce^{4+}, whereas peak B was assigned to Ce^{3+}. (b) Time-resolved absorption edge intensities in Ce L_3-edge XANES spectra during the atmosphere switching between 3% O_2/He and 3% H_2/He every 5 min at 600 °C. Data were collected every 0.2 s for 3 min after changing the atmosphere. Black and red lines represent $Pt/Ce_{0.5}Zr_{0.5}O_2$ and $Pt/Ce_{0.5}Zr_{0.4}Ti_{0.1}O_2$, respectively.

The OSC values of $Ce_{0.5}Zr_{0.5-x}Ti_xO_2$ ($0 \leq x \leq 0.2$) were estimated from the weight losses recorded using thermogravimetric analysis (TGA) during the atmosphere switching between 5% O_2/N_2 and 5% H_2/N_2 every 5 min (Fig. 3a).

The weight losses and gains of the samples corresponded to the following reactions:

$$Ce_{0.5}Zr_{0.5-x}Ti_xO_2 + \delta H_2 \rightarrow Ce_{0.5}Zr_{0.5-x}Ti_xO_{2-\delta} + \delta H_2O \quad (1)$$

$$Ce_{0.5}Zr_{0.5-x}Ti_xO_{2-\delta} + \delta/2 O_2 \rightarrow Ce_{0.5}Zr_{0.5-x}Ti_xO_2 \quad (2)$$

Pt-loaded samples (1 wt% on a metal basis) were used to quickly saturate their weight changes. As shown in Fig. 3 and Table 1, $Pt/Ce_{0.5}Zr_{0.4}Ti_{0.1}O_2$ and $Pt/Ce_{0.5}Zr_{0.3}Ti_{0.2}O_2$ showed considerably higher OSCs than $Pt/Ce_{0.5}Zr_{0.5}O_2$ at every temperature. The fact that $Pt/Ce_{0.5}Zr_{0.4}Ti_{0.1}O_2$ and $Pt/Ce_{0.5}Zr_{0.3}Ti_{0.2}O_2$ exhibited nearly equal OSCs at 600 °C ($\delta = 0.219$ and 0.221, respectively) suggested that Ti would not directly contribute to their OSCs via a $Ti^{4+} \leftrightarrow Ti^{3+}$ redox. This assumption was also supported by the irreducible nature of Ti^{4+} in this temperature range.[22] Fractions of reducible Ce^{4+} ($[Ce^{3+}]/[Ce^{3+}] + [Ce^{4+}]$) based on the theoretical maximum δ value of 0.25 (Table 1) were calculated to be 66.2%, 87.7%, and 88.4% for $Pt/Ce_{0.5}Zr_{0.5}O_2$, $Pt/Ce_{0.5}Zr_{0.4}Ti_{0.1}O_2$, and $Pt/Ce_{0.5}Zr_{0.3}Ti_{0.2}O_2$, respectively. These values clearly indicate that the high OSCs of $Pt/Ce_{0.5}Zr_{0.4}Ti_{0.1}O_2$ and $Pt/Ce_{0.5}Zr_{0.3}Ti_{0.2}O_2$ originate from the increase in the fraction of reducible Ce^{4+}.

Ce L_3-edge X-ray absorption near edge structure (XANES) spectra of $Pt/Ce_{0.5}Zr_{0.5}O_2$ and $Pt/Ce_{0.5}Zr_{0.4}Ti_{0.1}O_2$ at 600 °C in 3% O_2/He (Fig. 4a) showed two absorption peaks, at 5730 and 5737 eV (marked as A_1 and A_2), which were assigned to the Ce^{4+} species. These results were in agreement with the CeO_2 (Ce^{4+}) reference spectrum (Fig. S2, ESI†).[23] In 3% H_2/He, only one absorption peak, at 5726 eV (marked as B), assigned to the Ce^{3+} species (shown in the $Ce(NO_3)_3 \cdot 6H_2O$ (Ce^{3+}) reference) was observed, which indicated the reduction of Ce^{4+} species to Ce^{3+}. Moreover, in 3% H_2/He the absorption of $Pt/Ce_{0.5}Zr_{0.4}Ti_{0.1}O_2$ at B was higher than that of $Pt/Ce_{0.5}Zr_{0.5}O_2$, while in 3% O_2/He both samples showed almost the same absorption intensities. This result indicated that the fraction of reducible Ce^{4+} in $Pt/Ce_{0.5}Zr_{0.4}Ti_{0.1}O_2$ was higher than that in $Pt/Ce_{0.5}Zr_{0.5}O_2$, which was in agreement with the TGA results (Fig. 3b). The transient response of the
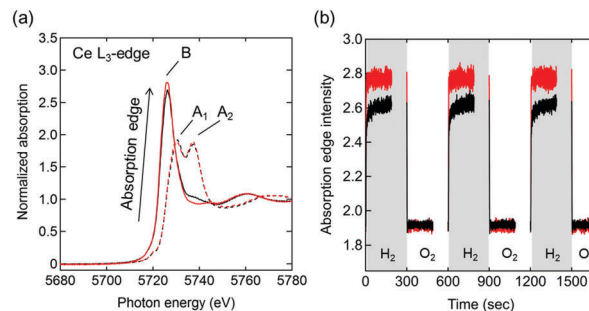
peak height of the absorption edge during the switching between 3% H_2/He and 3% O_2/He (Fig. 4b and Fig. S3, ESI†) suggested that the Ce^{4+} reduction rate in $Pt/Ce_{0.5}Zr_{0.4}Ti_{0.1}O_2$ was higher than that in $Pt/Ce_{0.5}Zr_{0.5}O_2$. For both samples, the intensities that increased in 3% H_2/He immediately returned to the original intensities when the atmosphere was changed to 3% O_2/He. This demonstrates that the reduced Ce^{3+} species were reversely re-oxidized to Ce^{4+} with high reproducibility.

The high OSCs of $Pt/Ce_{0.5}Zr_{0.4}Ti_{0.1}O_2$ could have originated from the topotactic transformation of the $Ce_{0.5}Zr_{0.4}Ti_{0.1}O_2$ into $Ce_{0.5}Zr_{0.4}Ti_{0.1}O_{1.75}$ pyrochlore. Bond valence sums (BVSs)[24,25] are often used to estimate the bond strengths of specific anion sites in crystals.[26,27] The respective BVSs of all the oxygen sites in $Ce_{0.5}Zr_{0.4}Ti_{0.1}O_2$ (marked as O1–O6; Fig. S4, ESI†) were obtained, and the $OZr(Ti)_4$ tetrahedron sites (O3 site: −1.61, O4 site: −1.37) were found to have larger values than the other O sites (from −1.82 to −2.46; Table S2, ESI†). The larger BVS values of the O3 and O4 sites suggested that the oxygen atoms at these sites were easily released, which caused the topotactic transformation of the $Ce_{0.5}Zr_{0.4}Ti_{0.1}O_2$ (Ce^{4+}) into $Ce_{0.5}Zr_{0.4}Ti_{0.1}O_{1.75}$ (Ce^{3+}) pyrochlore. These conclusions were in agreement with the results from κ-$Ce_2Zr_2O_8$ (Ce^{4+}), which was topotactically reduced to the $Ce_2Zr_2O_7$ (Ce^{3+}) pyrochlore with the release of oxygen atoms at the O3 and O4 sites (Fig. S4, ESI†).[28]

Interestingly, the OSC value of $Pt/Ce_{0.5}Zr_{0.4}Ti_{0.1}O_2$ (1310 μmol-O per g) at a lower temperature (200 °C) was approximately twice that of Pt/κ-$Ce_2Zr_2O_8$ (650 μmol-O per g, Fig. 5a). In contrast, the OSC values of both compounds above 400 °C were almost the same (1530–1560 μmol-O per g; Table 1 and Fig. S5, ESI†). Prolonging the reduction period (120 min) for Pt/κ-$Ce_2Zr_2O_8$ at 200 °C gave an OSC value of 740 μmol-O per g (Fig. S6, ESI†), which is still smaller than that of $Pt/Ce_{0.5}Zr_{0.4}Ti_{0.1}O_2$. This suggests that another factor other than SSA would determine the high OSC of $Pt/Ce_{0.5}Zr_{0.4}Ti_{0.1}O_2$. As shown in Fig. 5b and c, the BVS value of the O4 site in $Ce_{0.5}Zr_{0.4}Ti_{0.1}O_2$ (−1.37) was larger than that in κ-$Ce_2Zr_2O_8$ (−1.68), while the O3 sites in both had similar BVS values (−1.61 for $Ce_{0.5}Zr_{0.4}Ti_{0.1}O_2$
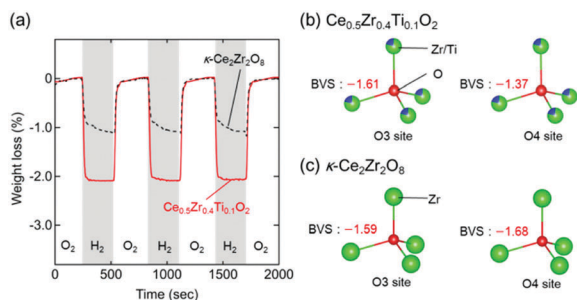
Fig. 5 (a) TGA curves of Pt/Ce$_{0.5}$Zr$_{0.4}$Ti$_{0.1}$O$_2$ (black dashed line) and Pt/κ-Ce$_2$Zr$_2$O$_8$ (red solid line) during the atmosphere switching between 5% O$_2$/N$_2$ and 5% H$_2$/N$_2$ every 5 min at 200 °C. BVS values of the O3 and O4 sites in (b) Ce$_{0.5}$Zr$_{0.4}$Ti$_{0.1}$O$_2$ and (c) κ-Ce$_2$Zr$_2$O$_8$.

and −1.59 for κ-Ce$_2$Zr$_2$O$_8$). The larger BVS value of the O4 site in Ce$_{0.5}$Zr$_{0.4}$Ti$_{0.1}$O$_2$ indicates that the oxygen atoms at this site were more weakly bound to the surrounding cations. The presence of such weakly bound oxygen atoms in Ce$_{0.5}$Zr$_{0.4}$Ti$_{0.1}$O$_2$ would decrease the oxygen vacancy formation energy, leading to a high OSC even at a lower temperature (200 °C).

In conclusion, Ce$_{0.5}$Zr$_{0.5-x}$Ti$_x$O$_2$ ($0 \leq x \leq 0.2$) were successfully synthesized *via* the solution combustion method. The substitution of Ti in Ce$_{0.5}$Zr$_{0.5}$O$_2$ induced pyrochlore-type cation ordering due to the increased cation size mismatch between the Ce and Zr sites, which caused a significant enhancement of the OSC. The most remarkable observation for the cation-ordered Ce$_{0.5}$Zr$_{0.4}$Ti$_{0.1}$O$_2$ was its high OSC (1310 μmol-O per g) even at a lower temperature (200 °C), which was twice that of conventional κ-Ce$_2$Zr$_2$O$_8$ (650 μmol-O per g). The high OSC at low temperature was explained by the formation of weakly bound oxygen atoms. This study demonstrated that an appropriate compositional control of Ce$_{0.5}$Zr$_{0.5}$O$_2$ allows for the induction of pyrochlore-type cation ordering without a high-temperature reduction. Future investigations of the various applications and catalytic activity of these cation-ordered materials synthesized *via* the solution combustion strategy would be of high interest.

Conflicts of interest

There are no conflicts of interest to declare.

Notes and references

1 (a) M. Yashima, *Catal. Today*, 2015, **253**, 3; (b) M. Karppinen, H. Yamauchi, S. Otani, T. Fujita, T. Motohashi, Y.-H. Huang, M. Valkeapää and H. Fjellvåg, *Chem. Mater.*, 2006, **18**, 490; (c) S. Remsen and B. Dabrowski, *Chem. Mater.*, 2011, **23**, 3818; (d) T. Motohashi, Y. Hirano, Y. Masubuchi, K. Oshima, T. Setoyama and S. Kikkawa, *Chem. Mater.*, 2013, **25**, 372; (e) A. Demizu, K. Beppu, S. Hosokawa, K. Kato, H. Asakura, K. Teramura and T. Tanaka, *J. Phys. Chem. C*, 2017, **121**, 19358.
2 Z. Xu, Z. Qi and A. Kaufman, *Power Sources*, 2003, **115**, 40.
3 W. C. Chueh, C. Falter, M. Abbott, D. Scipio, P. Furler, S. M. Haile and A. Steinfeld, *Science*, 2010, **330**, 1797.
4 C. M. Kalamaras, D. D. Dionysiou and A. M. Efstathiou, *ACS Catal.*, 2012, **2**, 2729.
5 A. F. Diwell, R. R. Rajaram, H. A. Shaw and T. J. Truex, *Stud. Surf. Sci. Catal.*, 1991, **71**, 139.
6 J. Kašpar and P. Fornasiero, *J. Solid State Chem.*, 2003, **171**, 19.
7 S. Otsuka-Yao-Matsuo, T. Omata, N. Izu and H. Kishimoto, *J. Solid State Chem.*, 1998, **138**, 47.
8 A. Suda, Y. Ukyo, H. Sobukawa and M. Sugiura, *J. Ceram. Soc. Jpn.*, 2002, **110**, 126.
9 Y. Nagai, T. Yamamoto, T. Tanaka, S. Yoshida, T. Nonaka, T. Okamoto, A. Suda and M. Sugiura, *Catal. Today*, 2002, **74**, 225.
10 H. Kishimoto, T. Omata, S. Otsuka-Yao-Matsuo, K. Ueda, H. Hosono and H. Kawazoe, *J. Alloys Compd.*, 2000, **312**, 94.
11 H.-F. Wang, Y.-L. Guo, G.-Z. Lu and P. Hu, *Angew. Chem., Int. Ed.*, 2009, **48**, 8289.
12 D. P. Reid, M. C. Stennett and N. C. Hyatt, *J. Solid State Chem.*, 2012, **191**, 2.
13 C. Heremans, B. J. Wuensch, J. K. Stalick and E. Prince, *J. Solid State Chem.*, 1995, **117**, 108.
14 G. King and P. M. Woodward, *J. Mater. Chem.*, 2010, **20**, 5785.
15 R. D. Shannon, *Acta Crystallogr., Sect. A: Cryst. Phys., Diffr., Theor. Gen. Crystallogr.*, 1976, **32**, 751.
16 B. D. Mukri, U. V. Waghmare and M. S. Hegde, *Chem. Mater.*, 2013, **25**, 3822.
17 B. Murugan, A. V. Ramaswamy, D. Srinivas and C. S. Gopinath, *Chem. Mater.*, 2005, **17**, 3983.
18 A. A. Saad, W. Khan, P. Dhiman, A. H. Naqvi and M. Singh, *Electron. Mater. Lett.*, 2013, **9**, 77.
19 M. S. Hegde, G. Madras and K. C. Patil, *Acc. Chem. Res.*, 2009, **42**, 704.
20 A. Varma, A. S. Mukasyan, A. S. Rogachev and K. V. Manukyan, *Chem. Rev.*, 2016, **116**, 14493.
21 S. F. Pal'guev, S. I. Alyamovskii and Z. S. Volchenkova, *Russ. J. Inorg. Chem.*, 1959, **4**, 1185.
22 B. Xu, H. Y. Sohn, Y. Mohassab and Y. Lan, *RSC Adv.*, 2016, **6**, 79706.
23 J. El Fallah, S. Boujana, H. Dexpert, A. Kiennemann, J. Majerus, O. Touret, F. Villain and F. Le Normand, *J. Phys. Chem.*, 1994, **98**, 5522.
24 I. D. Brown and D. Altermatt, *Acta Crystallogr., Sect. B: Struct. Sci.*, 1985, **41**, 244.
25 N. E. Brese and M. O'Keeffe, *Acta Crystallogr., Sect. B: Struct. Sci.*, 1991, **47**, 192.
26 A. Gupta, A. Kumar, U. V. Waghmare and M. S. Hegde, *J. Phys. Chem. C*, 2017, **121**, 1803.
27 N. Wakiya, K. Shinozaki, N. Mizutani and N. Ishizawa, *J. Am. Ceram. Soc.*, 1997, **80**, 3217.
28 S. N. Achary, S. K. Sali, N. K. Kulkarni, P. S. R. Krishna, A. B. Shinde and A. K. Tyagi, *Chem. Mater.*, 2009, **21**, 5848.